Article

Spatial Variability during Shrinkage Testing of Expansive Clays

Rajeevkaran Paranthaman [ID], Jared Suchan [ID] and Shahid Azam *[ID]

Environmental Systems Engineering, Faculty of Engineering and Applied Science, University of Regina, 3737 Wascana Parkway, Regina, SK S4S 0A2, Canada
* Correspondence: shahid.azam@uregina.ca

Abstract: Civil infrastructure constructed with, buried in, or underlain by expansive clays is affected by high volumetric changes, especially because large-scale facilities are spatially distributed. This research focused on determining spatial variability during the shrinkage testing of expansive clays. An initially saturated sample (600 mm in diameter) of a high-plasticity clay was exposed to desiccation and thoroughly monitored over five months. The results indicated an expansive clay (30% smectite and 14% illite) in alkaline-pore water (695 mg/L Na^+ and 1150 mg/L SO_4^{2-}) for developing a dispersive soil fabric. The vertical shrinkage in the intact-soil portion was unchanged (remaining at 114×10^6 mm^3) in the first 10 days, sharply decreased the initial volume by 30% (up to 280 mm or 80×10^6 mm^3) in 68 days, and slowly decreased the initial volume by 40% (up to 240 mm or 68×10^6 mm^3) in 145 days. Furthermore, the soil temperature was found to be 10% lower than the air temperature, whereas the relative humidity within the cell was found to be 30% higher than that outside the cell. The soil showed an initial prominent central ridge with a few cracks that gradually evolved into a distinct crack pattern with equal-sized and irregular soil chunks. The average soil surface showed no volume reduction up to 18 days and a subsequent linear reduction, reaching 25% of the initial soil volume by the end of the test.

Keywords: expansive clays; spatial variability; soil shrinkage; large cell

1. Introduction

Expansive clays are frequently encountered across arid and semi-arid regions of the world [1] including Australia, Canada, China, India, South Africa, the United Kingdom, and the United States of America. These soils comprise active clay minerals, such as smectite, and various forms of hydrous mica, which are derived from the conversion of feldspars in marine environments containing Na^+, K^+, Ca^{2+}, Mg^{2+}, CO_3^{2-}, Cl^-, and SO_4^{2-}, low precipitation, and restrained leaching [2–4]. The clay minerals exhibit swelling during infiltration and shrinkage during evaporation. Alternate deformations in surface soils cause distress to civil infrastructures, resulting in monetary losses associated with rehabilitation [5,6]. For example, the annual damages due to expansive clays in China and the United States of America add up to USD 30 billion [7]. A specific example of damage to infrastructure is that of Regina (Canada), where the average water-mains breaks are reported to be 243/year in the 900-km-long water-supply-pipeline network [8,9].

Shrinkage in expansive clays occurs due to the removal of capillary water from pore spaces in the soil matrix, as well as the adsorbed water on the clay particles [10,11]. Such deformations are spatially variable, that is, they occur in both vertical and lateral directions and are found at depths of up to about 3 m [12,13]. Moreover, these volumetric changes are associated with the development of cracks that are wide and numerous at the surface and gradually narrow down and diminish with depth [14,15]. The soil discontinuities are generally visible on the ground during periods of no rain and can become quite conspicuous under intensified and long-term desiccation due, for example, to large trees [16,17] and heating pipes [18,19]. The resulting subsidence affects the integrity of the

surface infrastructure (buildings and roads) and underground utilities (pipeline systems and storage tanks).

Laboratory methods for shrinkage determination can be divided into two groups. The one-dimensional methods, such as the linear-shrinkage-strain test [20], the consistency-limit test [21], and the linear-shrinkage-bar test [22], are limited by their reliance on linear measurement in rigid containers and low soil volumes to represent the field deposits. Similarly, the three-dimensional methods, using Vernier calipers [23] for vertical and lateral shrinkage or wax [24] for volumetric shrinkage, include the cracks volume, thereby underestimating changes in bulk volume. Digital-image-processing methods have been used to analyze crack patterns (width, depth, spacing) and crack progression in small samples [25,26] that are affected by the mechanical constraints at the specimen–container interface [27,28]. The use of large soil samples reduces the boundary effects, thereby facilitating the accurate capture of progressive changes in crack patterns and bulk volume during soil desiccation.

The main objective of this paper was to determine the spatial variability during the shrinkage testing of expansive clays. The soil deposit was surveyed and the materials were characterized for mineralogical and pore-water composition. The clay sample (which underwent free swelling in a large cell [29]) was exposed to desiccation and vertical deformations (along with air temperature, relative humidity, and soil temperature) were monitored over five months along the circumference. To determine the various components of the shrinkage, three-dimensional sample models were developed at critical time intervals using photogrammetry.
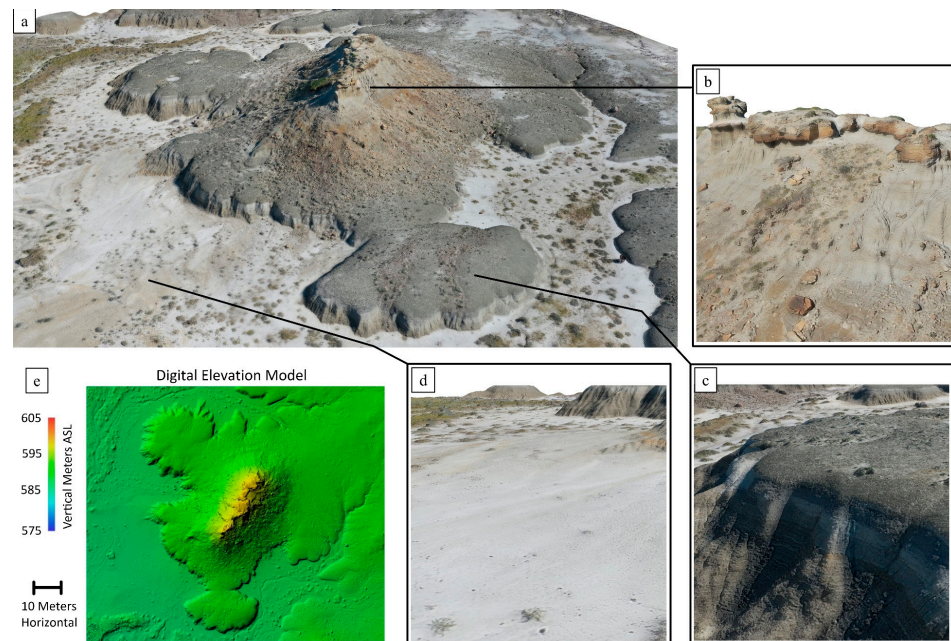
2. Research Methodology

2.1. Site Investigation and Sample Selection

The interaction of geologic setting with climatic conditions governs the mineral composition and the swelling–shrinkage behavior of soils. Figure 1 presents an overview of the investigated area in southern Saskatchewan, Canada. The site visit was conducted on 12 August 2021 after 3 days of 24 mm of rainfall in the area. During the visit, about 450 aerial photographs were taken through an unmanned aerial vehicle (UAV; Mavic 2 Pro manufactured by DJI, Shenzhen, China). The images were processed using the newly developed photogrammetry method by Suchan and Azam [30] with photogrammetry software (Agisoft Metashape Professional version 2.0) to develop the physical model (1.51 cm/pix) and the digital-elevation model (2.04 cm/pix) by aligning these in a three-dimensional space using longitude, latitude, and elevation.

Figure 1 shows three different materials in an 18-m vertical stratigraphic succession, namely: sandstone, mudrock, and pediment. As can be typically found in arid regions, the geomorphology of the deposit is derived from glacial geology and gradually evolved under the prevalent climatic conditions to the present-day sediments [31]. At the investigated site, the sandstone was the uppermost layer (from 592 m to 605 m above sea level (ASL)), occurring as tall rock pillars with concretionary caps. The mudrock was at the middle lithology (from 588 m to 592 m ASL) and appeared as alternating layers of fine-grained material with disintegrable popcorn-like surface features. This expansive clay is considered to be derived from pre-existing argillaceous rocks in marine environments [3,32]. The material is characterized by the presence of active clay minerals, including smectite, illite, and chlorite [31]. The pediment was the lowest sediment (from 587 m and 588 m ASL) and appeared to be freshly deposited from its smooth surface. During precipitation, the popcorn-like features swell to seal off the surface, resulting in runoff of most the water [33]. The surface water carries the eroded particles from the upper sandstone and deposits these at the pediment. The impermeable cover precludes trapping of the fine materials to ensure that the mudrock remains homogeneous irrespective of climatic conditions. Further details about the geology and hydrology of the area were provided by Imumorin and Azam [31] and Azam and Khan [33].

The selected expansive soil was popcorn-like material that was easily retrieved from the surface of the mudrock during the site visit. According to Khan and Azam [34], this clay is classified as highly plastic (CH) because it is fine-grained (97% of material is finer than 0.075 mm and 72% of material is finer than 0.002 mm) and has high consistency limits (liquid limit of 180% and plastic limit of 60%). Using the plasticity chart, the shrinkage limit of the clay was estimated to be 20% [35].

Figure 1. Survey of the investigated site: (**a**) panoramic overview; (**b**) sandstone; (**c**) mudrock; (**d**) pediment; and (**e**) digital-elevation model.

2.2. Soil and Water Composition

Soil composition was determined using a representative sample obtained from the mudrock surface comprising a homogenous material. An X-ray diffraction (XRD) analysis was conducted using a diffractometer (D4 Endeavor manufactured by Bruker, Coventry, UK) equipped with a monochromatic incident beam (Co K-alpha) at 35 kV and 40 mA. About 3 g of soil (<0.075 mm) was mixed in $Na_6[(PO_3)_6]$ solution. This mix was centrifuged at 600 rpm for 5 min to separate coarse particles (>0.002 mm) for random-orientation test and the remainder at 3000 rpm for 20 min to settle clay particles (<0.002 mm) for preferential-orientation test. The latter sample was examined under air-dried state as base case, $(CH_2OH)_2$-solvated for expansive clay minerals, and HCl-solvated for soluble clay minerals. All samples were scanned from 3° to 75° at a speed of 1° 2θ/min. To identify the minerals, the diffraction patterns were compared with Powder Diffraction File (PDF)-4 Mineral Database from the International Centre for Diffraction Data (ICDD). To quantify the minerals, the reference intensity ratio (RIR) method was used [36].

Exchangeable Na^+, K^+, Ca^{2+}, and Mg^{2+} were measured through inductively coupled plasma–optical emission spectroscopy (ICP–OES). About 10 g of soil was mixed with 40 mL of 1 M $C_2H_7NO_2$, agitated in a reciprocal shaker, and filtered after 24 h via Buchner funnel using Whatman No. 42 filter paper (manufactured by Whatman International, London, UK) [37]. A solution extract was injected into ICP–OES (Optima 7300s manufactured by PerkinElmer, Waltham, MA, USA), heated up to 7000 °C and allowed to cool down. The emitted light wavelengths were used for cation identification, whereas the spectroscopic intensity was used for cation quantification. The sum of all ions was reported as cation-exchange capacity (CEC).

Thermo-gravimetric analysis (TGA) was conducted to identify mineral changes and soil-water loss. About 10 g of powdered soil (finer than 0.0075 mm) was placed in the
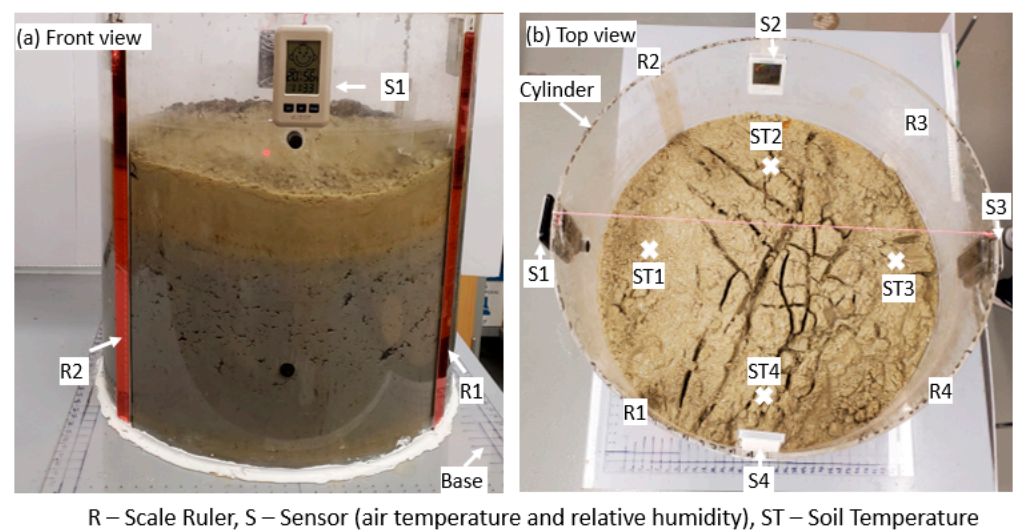
analyzer (TGA 701 manufactured by LECO, ST Joseph, MO, USA) and the temperature was raised from 28 °C (ambient) to 950 °C at a rate of 2 °C/min. The weight loss during thermal increase was recorded. To minimize oxidation, the analyzer was initially purged with nitrogen (N_2) and a gas flow of 7 L/min was retained throughout the test.

To assess the shrinkage behavior due to clay–liquid interactions, composition of the pore water was determined on the water released from the saturated soil in the large cell, after removing the surplus water. The concentrations of Na^+, K^+, Mg^{2+}, and Ca^{2+} were obtained by the standard methods for plasma emission spectroscopy–inductively coupled plasma (PES-ICP) method (SM 3120 B) using PerkinElmer Optima 7300s. Similarly, the standard methods for determination of anions by ion chromatography (SM 4110B developed by National Water Quality Monitoring Council, Syracuse, USA) were used to determine the concentrations of CO_3^{2-}, HCO_3^-, Cl^-, NO_3^-, and SO_4^{2-} using ICS-1000 Chromatography System (manufactured by Dionex, Sunnyvale, CA, USA).

2.3. Shrinkage Monitoring and Sample Modeling

The shrinkage test was conducted on the clay sample (water content = 205%), which had undergone free swelling in a large cell for more than 6 years. The sample was initially prepared by gently tapping with a rubber mallet to attain a homogeneous-field dry density of 1.1 g/cm^3 with a water content of 25%. Details about the sample preparation method are described in Khan and Azam [38]. Figure 2 shows the instrumented large cell (cross-sectional area of 283×10^3 mm^2) containing the sample. The sample was allowed to desiccate under ambient laboratory conditions after undergoing swelling for more than eight years. To measure the soil–cell contact height (CH), four scale rulers (R1, R2, R3, and R4) were attached along the cell circumference on the outer side of the wall. These heights represent vertical shrinkage in the intact portion of the saturated soil in the large cell. The laboratory conditions (air temperature and relative humidity) were monitored at two internal (S2 and S4) and two external (S1 and S3) points along the circumference of the cell using the digital-humidity and temperature-monitor sensors (K0721 manufactured by La Crosse Technology, La Crosse, WI, USA). The soil temperature (ST) was monitored at four locations (ST1, ST2, ST3, and ST4) using non-contact infrared temperature measurement (Infrared Thermometer with Mildew Alarm manufactured by MAXIMUM, Shanghai, China). All readings (contact height, air temperature, relative humidity, and soil temperature) were simultaneously recorded every day for initial 7 days, every 2 days for next 14 days, and every 3 days thereafter. These periods of measurements corresponded with significant volumetric changes and were based on visual observations.

R – Scale Ruler, S – Sensor (air temperature and relative humidity), ST – Soil Temperature

Figure 2. Photographs of instrumented large cell containing the expansive clay: (**a**) front view; (**b**) top view.
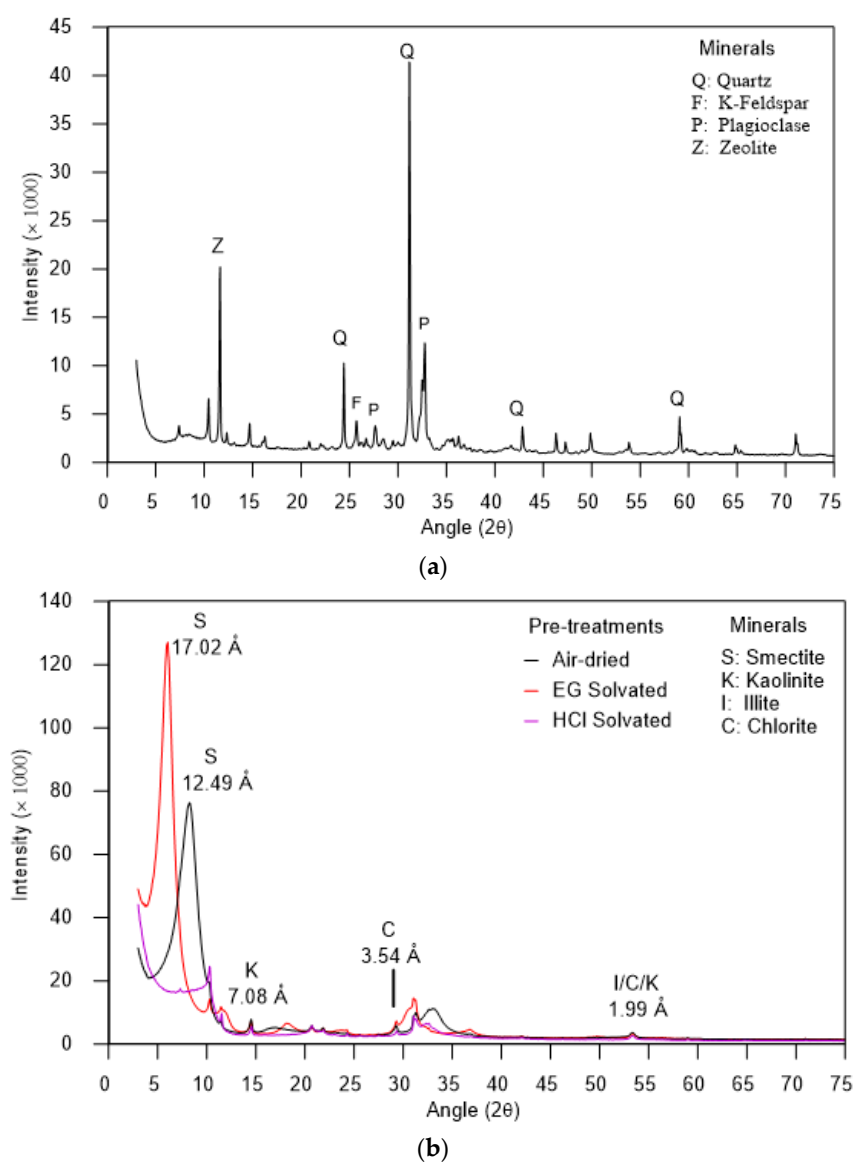
Three-dimensional soil models were developed when significant shrinkage was observed in the sample, using the newly developed photogrammetry method [30]. About 200 photographs were captured at various points around the sample using a cellphone camera (Samsung S10 manufactured by Samsung Electonics, Yeongtong-gu, South Korea). Four calibrated controlled points, situated on the exterior walls of the cell, were manually identified in each image in the photogrammetry software (Agisoft Metashape Professional). After image alignment, the depth maps were used to create dense point clouds, which, in turn, were cleaned to remove unwanted points. The clouds were converted into 3D mesh models, imported into a drafting computer software (Trimble SketchUp version 5.0.0), and combined with a simulated version of the large cell interior. The "precise perimeter" of the soil surface was created using the intersect function. The 3D mesh model was also imported into a point-cloud software (GPL CloudCompare version 2) and the exposed soil surface was extracted using the "precise perimeter". The bulk soil volume and digital-elevation models (DEMs) were determined by importing the simulated version of the large cell interior and using the "2.5D Volume Analysis" tool along with the exposed soil surface.
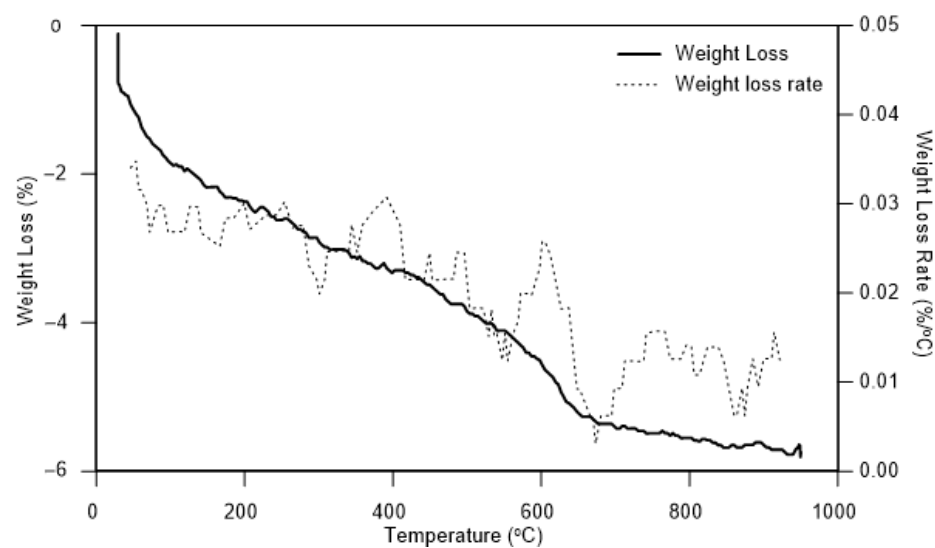
3. Results and Discussion

Figure 3 shows the X-ray diffraction patterns of the investigated expansive clay. The coarse sample (Figure 3a) showed distinct peaks of quartz at 24.4°, 31.2°, 42.9°, and 59.1°, thereby confirming the accuracy of the analyses for other minerals [2]. The quartz originated from the sandstone due to sheet and fluvial erosion [33]. The various types of feldspar (K-feldspar at 25.8° and plagioclase at 27.7° and 32.7°) are related to the deposition of volcanic debris in the Cretaceous period and subsequent weathering during the Quaternary. Low-temperature metamorphism also resulted in the secondary alteration of the volcanic debris to form zeolite, observable at 11.6° [39]. Similarly, clay minerals (Figure 3b) evolved from the feldspars under restrained leaching, extreme aridity, and an abundance of salt-forming ions [10,40]. The presence of smectite was validated by the peak shifting from 8.4° (air-dried) to 6.1° (EG-solvated) and by the absence of the first peak (HCl-solvated) due to mineral decomposition [40]. By contrast, the presence of kaolinite (14.4°) and chlorite (29.3°) was confirmed from the absence of shifts in the peaks for the EG-solvated and HCl-solvated samples. The presence of expansive clay minerals (smectite, illite, and chlorite) confirmed that the soil was an expansive clay. The investigated clay results were close to the results obtained by Khan [41] for the same soil, thereby confirming the homogeneity of the soil, as well as precluding the need to repeat the tests. Furthermore, these results have to be appreciated in light of the limitations of XRD, namely: the identification of amorphous materials, the appearance of non-crystalline materials as baseline noise, the degree of material crystallinity, and pertinent grain sizes [42].

Figure 4 gives the results of the TGA for the expansive clay, exhibiting a total weight loss of 5.7%. The weight-loss-rate curve shows the following distinct peaks: (i) a 3% reduction between 28 °C and 300 °C, due to the removal of adsorbed or interlayer water from the expansive clay minerals [43]; (ii) a 1% reduction between 300 °C and 550 °C, due to dehydration of the zeolite [44]; (iii) a 1.3% reduction between 550 °C and 680 °C, due to the removal of the hydroxyl ion from the kaolinite [40]; and (iv) a 0.4% reduction between 680 °C and 880 °C, due to the decomposition of the zeolite [44].

Table 1 gives a summary of the soil and water composition for the investigated expansive soil. The clay was found to comprise 47% coarse minerals (14% quartz, 20% zeolite, 7% plagioclase, and 3% feldspars) and 53% clay minerals (30% smectite, 14% illite, 7% chlorite, and 2% kaolinite). Furthermore, the CEC measured 42.5 cmol(+)/kg, with Na^+ and Ca^{2+} accounting for 94% of the total exchangeable cations. These data indicate Na^+–smectite as the predominant exchange complex associated with the high water adsorption on the clay surfaces. Furthermore, Na^+ (695 mg/L) and SO_4^{2-} (1150 mg/L) were found to be the major ions in the pore water, accounting for 82% of the total dissolved solids. The corresponding sodium-adsorption ratio (SAR) of 37.3 indicated a dispersive soil [2] that likely governed the popcorn-like clay structure in the field.

Figure 3. X-ray diffraction patterns for the investigated expansive clay: (**a**) coarse sample; (**b**) clay sample.

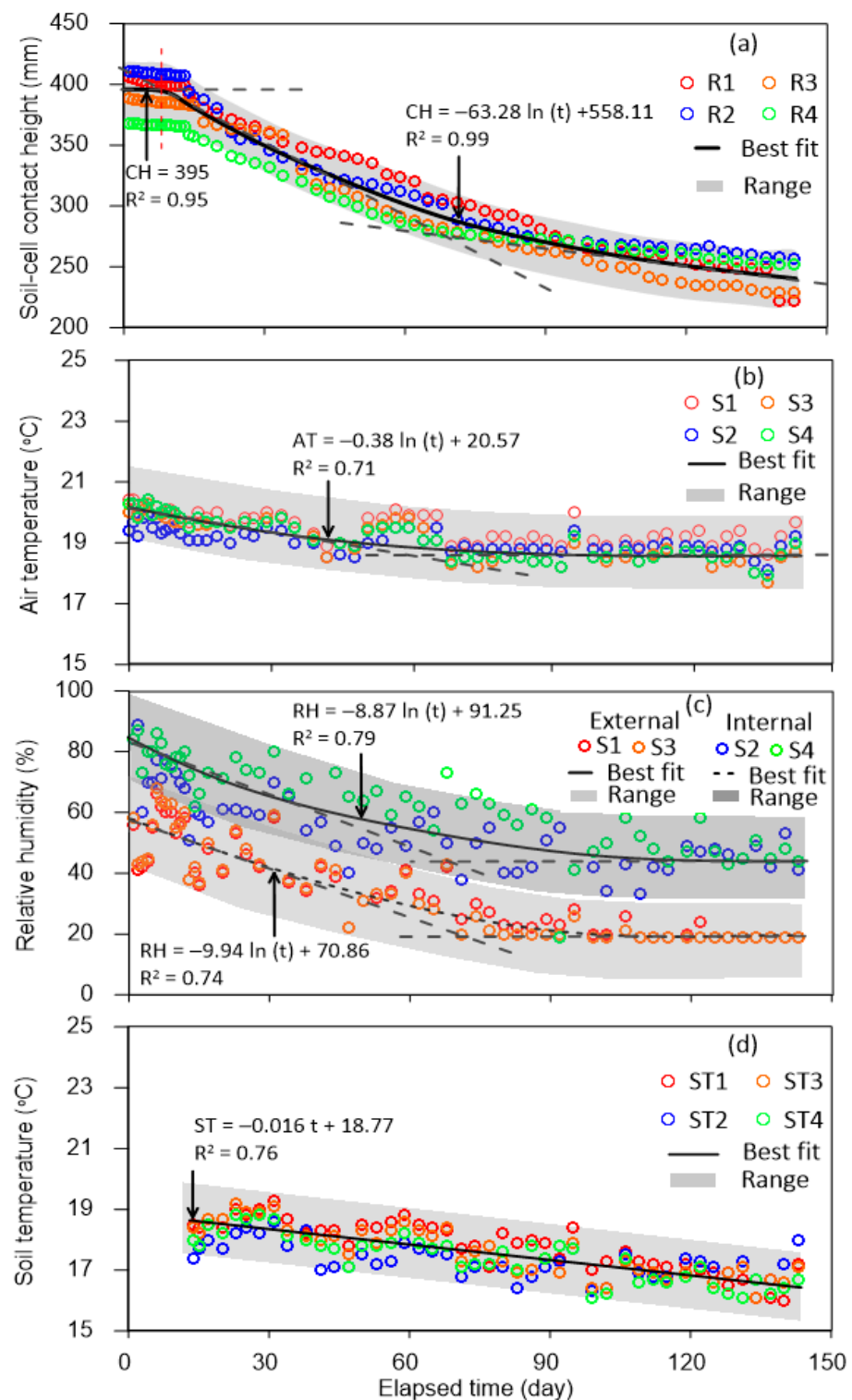**Figure 4.** Thermo-gravimetric analysis of the investigated expansive clay.

Table 1. Summary of soil and pore-water compositions.

Property	Value
Minerals (%) *	Coarse (47)
	Quartz (14), Zeolite (20), Plagioclase (7),
	K-Feldspar (3), Others (3)
	Clay (53)
	Smectite (30), Illite (14), Chlorite (7), Kaolinite (2)
Exchangeable cations (cmol(+)/kg)	Na^+ (22.7), K^+ (1.2), Ca^{2+} (17.2), Mg^{2+} (1.2)
Cation-exchange capacity (cmol(+)/kg)	42.5
Dissolved ions (mg/L)	Na^+ (695), K^+ (4.3), Ca^{2+} (21.2), Mg^{2+} (3.1), HCO_3^- (561),
	CO_3^{2-} (44), Cl^- (50.8), NO_3^- (2.2), SO_4^{2-} (1150)
Total dissolved solids (mg/L)	2250
Sodium-absorption ratio †	37.3

* Accuracy $\pm 1\%$, † $SAR = \dfrac{Na^+}{\sqrt{\frac{Mg^{2+}+Ca^{2+}}{2}}}$.

Figure 5 presents the transient changes during the shrinkage of the investigated expansive clay. The soil–cell contact-height data (Figure 5a) were found to vary by ± 20 mm of the best fit ($R^2 = 0.95$ for the initial straight-line portion and $R^2 = 0.99$ for the remaining logarithmic-curve portion). The best-fit curve showed three stages of volume reduction: (i) no change (remaining at 400 mm) in the first 10 days because of pore-water expulsion under saturated conditions; (ii) a sharp decrease from 400 mm to 280 mm up to the 68th day because of evaporation from the fully exposed soil surface; and (iii) a slow decrease from 280 mm to 240 mm up to the 145th day because of reduced evaporation due to partial coverage by the upper soil.

The air-temperature data (Figure 5b), from both the external and the internal sensors, was found to vary by ± 1 °C. The logarithmic best-fit curve ($R^2 = 0.71$) showed an initial decrease from 20.1 °C to 18.8 °C in the first 60 days and remained constant thereafter. The higher initial temperature was partly due to the convection oven (located 2 m away from the large cell), which was turned off during the remainder of the test. Similarly, the gradual temperature reduction over five months (from August to December) was also affected by the decreasing air temperature outside the laboratory building. The relative-humidity data (Figure 5c), showed identical trends for both the external and the internal sensors, with variations in the $\pm 15\%$ range. As before, the logarithmic best-fit curves ($R^2 = 0.74$ for the external sensors and $R^2 = 0.79$ for the internal sensors) showed an initial decrease up to 70 days (58% to 20% for external sensors 84% to 44% for internal sensors) and remained constant thereafter. This was attributed to the high level of evaporation from the initially saturated soil, which gradually reduced due to the increasing capillary forces, which tend to retain water under unsaturated conditions [45]. The higher average values inside the cell compared to the outside are attributable to the presence of water vapor above the soil in the cell, as well as the fact that the drying of the soil cooled the ambient air around the sample [46]. The soil-temperature data (Figure 5d) were not collected for the first 10 days to preclude the measurement errors due to the surface reflection and refraction of the laser by the water released from the saturated soil [47]. The retrieved data were found to best fit a linear equation ($R^2 = 0.76$) and varied by ± 1 °C. The average curve linearly decreased from 18.5 °C to 16.5 °C over the remainder of the test. This was attributed to the time-dependent conduction of the absorbed heat from the warm air to the soil surface.
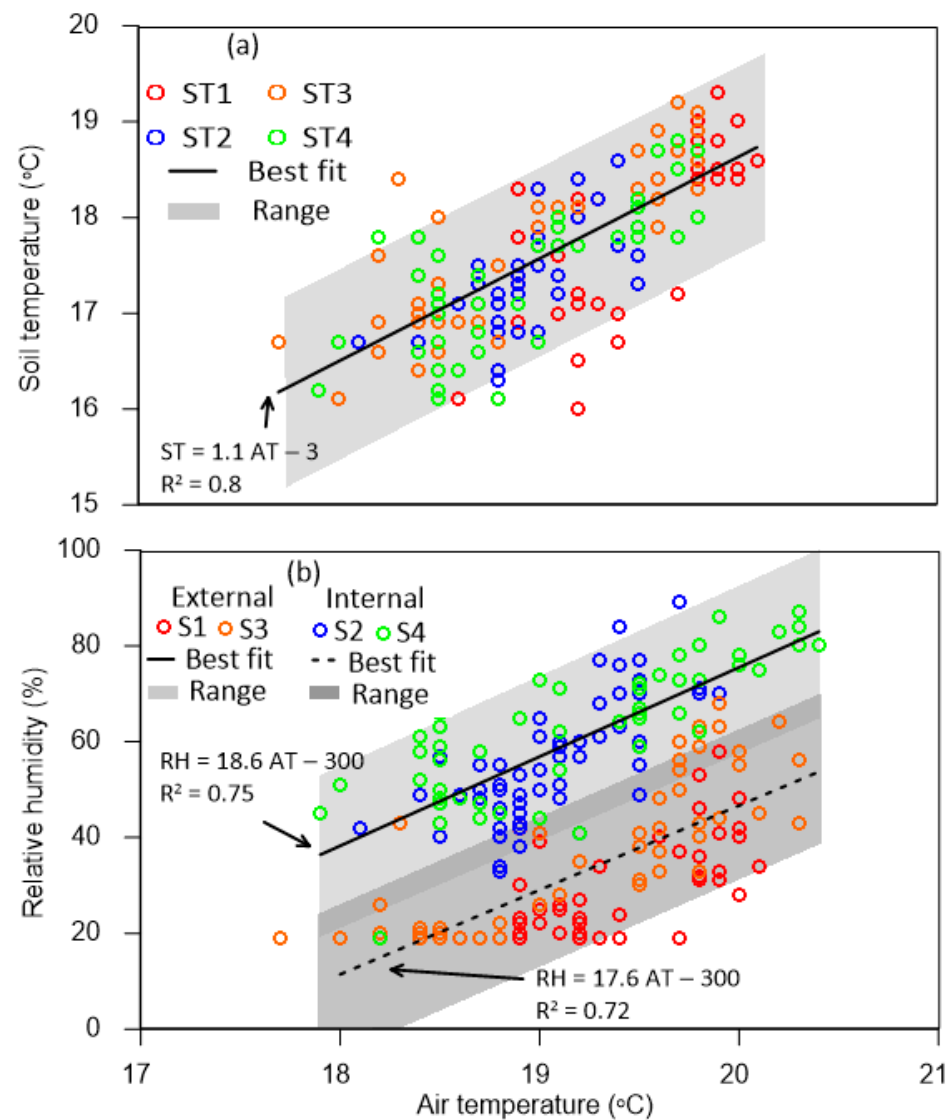
Figure 5. Transient changes during shrinkage test in large cell: (**a**) soil–cell contact height; (**b**) air temperature; (**c**) relative humidity; and (**d**) soil temperature.

Figure 6 shows the correlations of the soil temperature and relative humidity with the air temperature. The soil-temperature data (Figure 6a) were found to best fit a linear equation (R^2 = 0.8) with a range of ±1 °C. The soil temperature inside the cell was found to be 10% less than the air temperature recorded by both the external and the internal sensors. As mentioned above, the reduction corresponded to the instantaneous values of air temperature and soil temperature, that is, the latter equilibrated within the soil
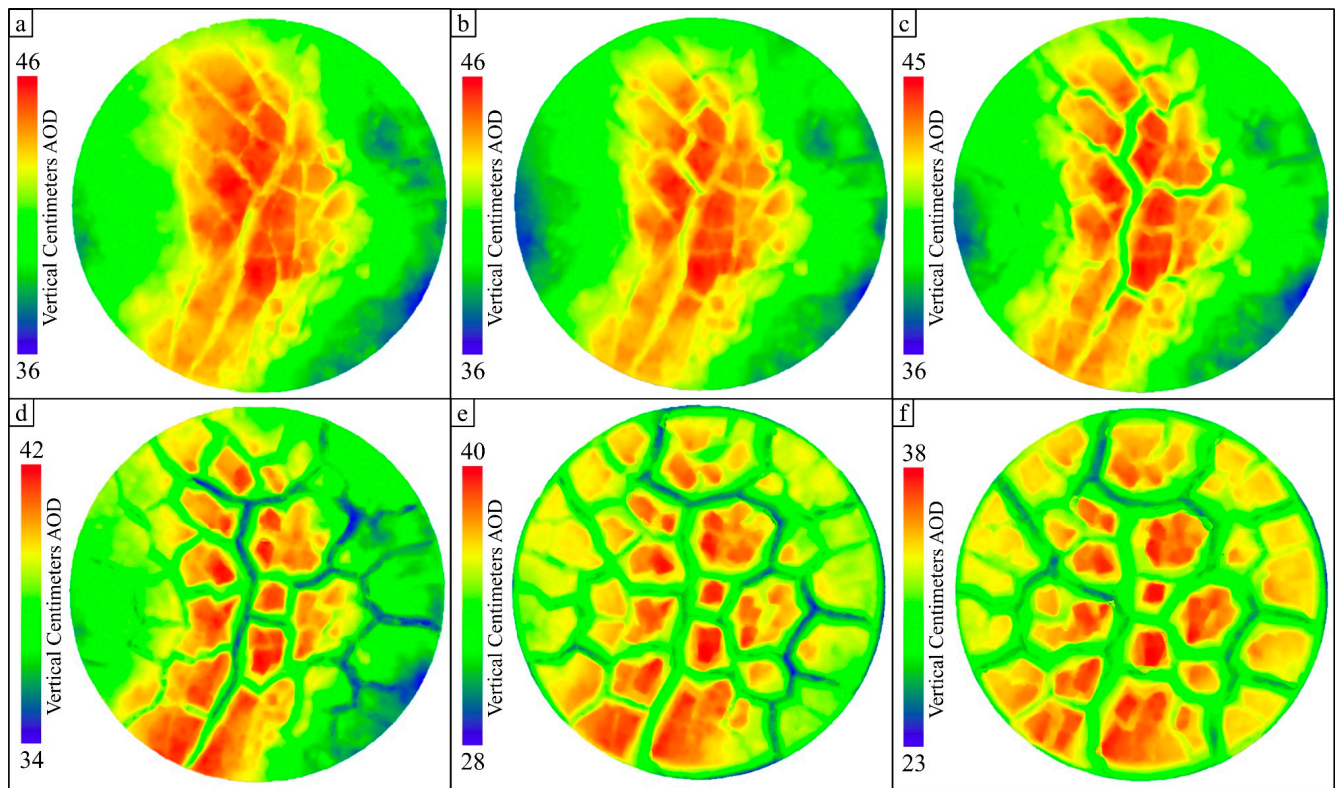
mass over time. The relative-humidity data (Figure 6b) were found to best fit a linear equation ($R^2 = 0.75$ for the external sensors and $R^2 = 0.72$ for the internal sensors). For the investigated range of air temperatures, the relative humidity inside the cell was found to be 30% higher than that outside the cell because of the above reasons.

Figure 6. Correlation of measured air temperature during shrinkage in the large cell (**a**) with soil temperature and (**b**) with relative humidity.

Figure 7 and Table 2 give the maximum crack depth (d_c) calculated using digital-elevation models of the soil surface. The 10-day (d_c of 3 cm) model showed a prominent and irregular ridge in the middle that covered about one-third of the sample. This feature developed during the preceding swelling, which was highest in the middle and lowest along the perimeter because of the soil–cell friction and lateral restraint of the cell [29]. The ridge also showed the initiation of a few cracks similar to the fissuring in an over-consolidated clay [48,49]. The 18-day (d_c of 5 cm) and the 40-day (d_c of 6 cm) models showed a gradual increase in the crack sizes and the development of distinct clusters, while the lower areas on either side of the ridge remained relatively unchanged. The 68-day (d_c of 7 cm) capture indicated a further increase in the crack dimensions along with the initiation of newer cracks away from the initial ridge. The 111-day (d_c of 11 cm) model showed lateral growth and intensified cracking throughout the sample and the start of soil detachment from the cell. The 143-day (d_c of 9 cm) model showed a fully developed crack

pattern along with equal-sized, albeit irregular shaped, soil chunks. At this stage, the ridge was non-existent and the average soil height was similar across the sample.
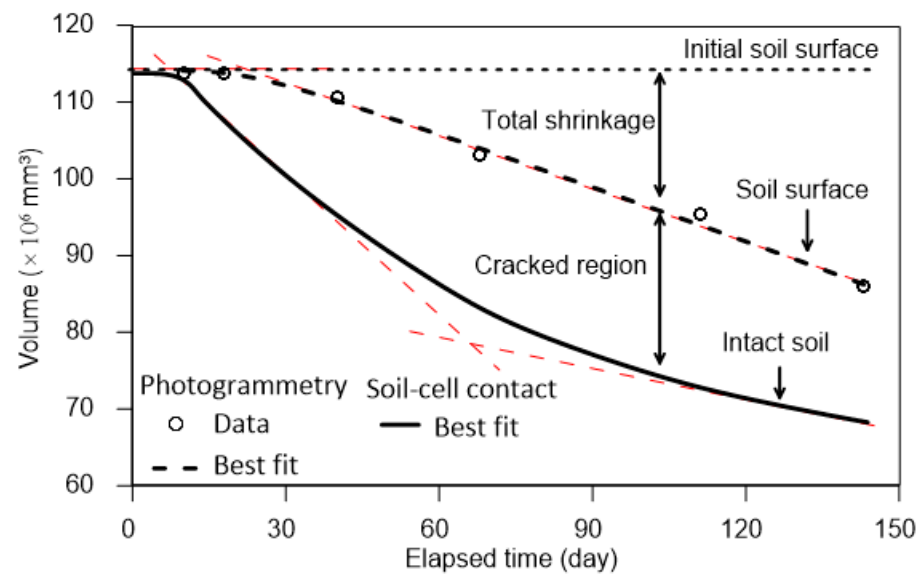

Figure 7. Digital-elevation models of the soil surface during shrinkage: (**a**) day 10; (**b**) day 18; (**c**) day 40; (**d**) day 68; (**e**) day 111; and (**f**) day 143.

Table 2. Summary of maximum crack depths calculated using digital-elevation models.

Days	Elevation of Soil Surface in the Middle (cm)	Elevation of Cracked Soil in the Middle (cm)	Maximum Crack Depth (cm)
10 (Figure 7a)	46 (red)	43 (yellow)	3
18 (Figure 7b)	46 (red)	41 (light green)	5
40 (Figure 7c)	45 (red)	39 (green)	6
68 (Figure 7d)	42 (red)	35 (dark purple)	7
111 (Figure 7e)	40 (red)	29 (light purple)	11
143 (Figure 7f)	38 (red)	29 (green)	9

Figure 8 compares the volumes based on the soil–cell contact measurements and photogrammetric models. The best-fit curve of the intact soil followed the curve given in Figure 5a. Based on the initial soil volume, the volume reductions were found to be zero after 10 days, 30% after 68 days, and 40% after 145 days. The best-fit curve of the average soil surface showed no volume reduction up to 18 days followed by a linear volume reduction, reaching 25% of the initial soil volume at the end of the test. The volume difference between the initial and transient soil surfaces represents the total shrinkage comprising both vertical and lateral deformations. Furthermore, the volume difference between the soil surface and the intact soil corresponded to the cracked region in the soil. This region was found to gradually increase, reaching 18×10^6 mm^3 at the end of the test. Three-dimensional photogrammetric models are useful in determining bulk soil volume and crack propagation during shrinkage. This method was found to be simple (since it requires a cellular-phone camera), quick (since it requires a short time for image capturing), and economical (since it requires mostly open-source computational software).

Figure 8. Comparison of photogrammetric volume and soil–cell contact volume.

The results of this investigation are similar to those of other published work on shrinkage testing. Udukumburage et al. [50] used a small circular sample (55 mm in diameter and 48 mm in height) of Kurita clay and Umezaki and Kawamura [51] used a large circular sample (400 mm in diameter and 1000 mm in height) of Sherwood clay. The transient-shrinkage plot showed a sharp decrease down to 25% of the initial volume in 13 days for the Kurita clay and in 40 days for the Sherwood clay. Thereafter, a slow decrease was reported for both materials: the Kurita clay reached a 30% volume decrease over 25 days, whereas the Sherwood clay achieved a 33% volume reduction in 160 days. The short time required for the drying of the former clay was due to the faster movement of the drying front through the smaller sample. The discrepancies between this study and the reported results using large-scale equipment are attributable to the following variables: (i) the ambient conditions of air temperature, air flow, relative humidity, and laboratory lighting; (ii) the sample size, height-to-diameter ratio, and container material; (iii) the use of different testing and analysis methods; and (iv) the sample composition and cracking patterns.

4. Summary and Conclusions

Knowledge of the spatial variability during shrinkage testing in expansive clays is critical for the integrity of civil infrastructure exposed to intensified and long-term desiccation. The main achievements of this research include the development of correlations between environmental conditions and soil desiccation and the successful implementation of photogrammetry to quantitatively determine soil shrinkage and qualitatively understand crack propagation over time. An initially saturated sample of a high-plasticity clay was exposed to desiccation in a large cell and thoroughly monitored over five months. The main conclusions of this research are summarized as follows:

- The selected clay comprised expansive minerals, such as smectite (30%) and illite (14%), and the pore water mainly showed the presence of Na^+ (695 mg/L) and SO_4^{2-} (1150 mg/L). With a cation-exchange capacity of 42.5 cmol(+)/kg, the predominant exchange complex was found to be Na^+-smectite, which is associated with a dispersive soil fabric.
- The vertical shrinkage in the intact-soil portion was unchanged (remaining at 114×10^6 mm^3) in the first 10 days because of pore-water expulsion, followed by a sharp decrease of up to 280 mm (80×10^6 mm^3) over 68 days because of surface

exposure and, subsequently, by a slow decrease down to 240 mm (68×10^6 mm^3) over 145 days because of partial coverage by the upper soil.

- The shrinkage behavior of the investigated expansive clay corroborated well with the ambient environmental parameters during the five-month test duration. The soil temperature inside the cell was found to be 10% lower than the air temperature, whereas the relative humidity within the cell was found to be 30% higher than that outside the cell.
- The soil initially showed a prominent central ridge with a few cracks that gradually evolved to a distinct crack pattern with equal-sized and irregular soil chunks. The average soil surface showed no volume reduction up to 18 days and a subsequent linear volume reduction, reaching 25% of the initial value by the end of the test.

Author Contributions: Laboratory testing and field investigations, R.P. and J.S.; writing—original draft, R.P and J.S.; conceptual guidance, S.A.; writing—review and editing, S.A. All authors have read and agreed to the published version of the manuscript.

Institutional Review Board Statement: Not applicable.

Informed Consent Statement: Not applicable.

Data Availability Statement: The data presented in this study are available in the figures and tables.

Conflicts of Interest: The authors declare no conflict of interest.

References

1. Mishra, A.K.; Dhawan, S.; Rao, S.M. Analysis of Swelling and Shrinkage Behavior of Compacted Clays. *Geotech. Geol. Eng.* **2008**, *26*, 289–298. [CrossRef]
2. Mitchell, J.K.; Soga, K. *Fundamentals of Soil Behavior*; John Wiley & Sons: New York, NY, USA, 2005.
3. Ito, M.; Azam, S. Engineering Characteristics of a Glacio-Lacustrine Clay Deposit in a Semi-Arid Climate. *Bull. Eng. Geol. Environ.* **2009**, *68*, 551–557. [CrossRef]
4. Hillel, D. *Environmental Soil Physics: Fundamentals, Applications, and Environmental Considerations*; Elsevier: Amsterdam, The Netherlands, 1998.
5. Hu, Y.; Hubble, D.W. Failure Conditions of Asbestos Cement Water Mains in Regina. In Proceedings of the 1st CSCE Specialty Conference on Infrastructure Technologies, Management and Policy, Toronto, ON, Canada, 2–4 June 2005; pp. 2–4.
6. Nelson, J.D.; Miller, D.J. *Expansive Soils: Problems and Practice in Foundation and Pavement Engineering*; John Wiley & Sons, Inc.: New York, NY, USA, 1992.
7. Li, J.; Cameron, D.A.; Ren, G. Case Study and Back Analysis of a Residential Building Damaged by Expansive Soils. *Comput. Geotech.* **2014**, *56*, 89–99. [CrossRef]
8. Hu, Y.; Vu, H.Q.; Lotfian, K. Instrumentation of a Section of AC Pipe in Expansive Soil. In *Pipelines 2008: Pipeline Asset Management: Maximizing Performance of Our Pipeline Infrastructure*; Curran Associates, Inc.: New York, NY, USA, 2008; pp. 1–10.
9. Paranthaman, R.; Azam, S. Coupled Hydraulic-Thermal Model for Soils under Extreme Weather in Cold Regions. *J. Environ. Inform. Lett.* **2022**, *7*, 90–102. [CrossRef]
10. Azam, S.; Shah, I.; Raghunandan, M.E.; Ito, M. Study on Swelling Properties of an Expansive Soil Deposit in Saskatchewan, Canada. *Bull. Eng. Geol. Environ.* **2013**, *72*, 25–35. [CrossRef]
11. Julina, M.; Thyagaraj, T. Quantification of Desiccation Cracks Using X-Ray Tomography for Tracing Shrinkage Path of Compacted Expansive Soil. *Acta Geotech.* **2019**, *14*, 35–56. [CrossRef]
12. Ito, M.; Azam, S.; Clifton, W. Suction-Based Model for Predicting Cyclic and Transient Volume Changes in Expansive Clays Using a Material Property Function. *Eng. Geol.* **2022**, *296*, 106491. [CrossRef]
13. Morris, P.H.; Graham, J.; Williams, D.J. Cracking in Drying Soils. *Can. Geotech. J.* **1992**, *29*, 263–277. [CrossRef]
14. Cordero, J.A.; Prat, P.C.; Ledesma, A. Experimental Analysis of Desiccation Cracks on a Clayey Silt from a Large-Scale Test in Natural Conditions. *Eng. Geol.* **2021**, *292*, 106256. [CrossRef]
15. Ito, M.; Azam, S. Relation between Flow through and Volumetric Changes in Natural Expansive Soils. *Eng. Geol.* **2020**, *279*, 105885. [CrossRef]
16. Bordoloi, S.; Hussain, R.; Gadi, V.K.; Bora, H.; Sahoo, L.; Karangat, R.; Garg, A.; Sreedeep, S. Monitoring Soil Cracking and Plant Parameters for a Mixed Grass Species. *Géotech. Lett.* **2018**, *8*, 49–55. [CrossRef]

17. Cameron, D.A. The Extent of Soil Desiccation near Trees in a Semi-Arid Environment. In *Unsaturated Soil Concepts and Their Application in Geotechnical Practice*; Toll, D.G., Ed.; Springer: Dordrecht, The Netherlands, 2001; pp. 357–370, ISBN 978-94-015-9775-3.

18. Kleiner, Y.; Rajani, B. Considering Time-Dependent Factors in the Statistical Prediction of Water Main Breaks. In Proceedings of the American Water Works Association Infrastructure Conference, Baltimore, MD, USA, 12–15 March 2000.

19. Yu, F.; Zhang, M.; Lai, Y.; Liu, Y.; Qi, J.; Yao, X. Crack Formation of a Highway Embankment Installed with Two-Phase Closed Thermosyphons in Permafrost Regions: Field Experiment and Geothermal Modelling. *Appl. Therm. Eng.* **2017**, *115*, 670–681. [CrossRef]

20. Puppala, A.J.; Katha, B.; Hoyos, L.R. Volumetric Shrinkage Strain Measurements in Expansive Soils Using Digital Imaging Technology. *Geotech. Test. J.* **2004**, *27*, 547–556.

21. *ASTM D4318-17*; Standard Test Methods for Liquid Limit, Plastic Limit, and Plasticity Index of Soils. Annual Book of ASTM Standards: West Conshohocken, PA, USA, 2017.

22. TxDOT. *Test Procedure for Determining the Bar Linear Shrinkage of Soils*; Texas Department of Transportation: Austin, TX, USA, 1999.

23. Tripathy, S.; Rao, K.S.; Fredlund, D.G. Water Content-Void Ratio Swell-Shrink Paths of Compacted Expansive Soils. *Can. Geotech. J.* **2002**, *39*, 938–959. [CrossRef]

24. *ASTM D4943-18*; Standard Test Method for Shrinkage Factors of Cohesive Soils by the Water Submersion Method. Annual Book of ASTM Standards: West Conshohocken, PA, USA, 2018.

25. Peron, H.; Hueckel, T.; Laloui, L.; Hu, L. Fundamentals of Desiccation Cracking of Fine-Grained Soils: Experimental Characterisation and Mechanisms Identification. *Can. Geotech. J.* **2009**, *46*, 1177–1201. [CrossRef]

26. Vogel, H.-J.; Hoffmann, H.; Leopold, A.; Roth, K. Studies of Crack Dynamics in Clay Soil: II. A Physically Based Model for Crack Formation. *Geoderma* **2005**, *125*, 213–223. [CrossRef]

27. Cuadrado, A.; Encalada López, D.A.; Ledesma Villalba, A.; Prat Catalán, P. Soil Surface Boundary Condition in Desiccating Soils. In Proceedings of the Conference Proceedings on Geotechnical Engineering, Foundation of the Future, Reykjavík, Iceland, 1–7 September 2019; The Icelandic Geotechnical Society (IGS): Reykjavík, Iceland; pp. 1–8.

28. Lakshmikantha, M.R.; Prat, P.C.; Ledesma, A. Boundary Effects in the Desiccation of Soil Layers with Controlled Environmental Conditions. *Geotech. Test. J.* **2018**, *41*, 675–697. [CrossRef]

29. Khan, F.S.; Azam, S. Spatial Variability in Swelling of Aggregated Expansive Clays. *Innov. Infrastruct. Solut.* **2016**, *1*, 11. [CrossRef]

30. Suchan, J.; Azam, S. Controlled Photogrammetry System for Determination of Volume and Surface Features in Soils. *MethodsX* **2021**, *8*, 101368. [CrossRef]

31. Imumorin, P.; Azam, S. Effect of Precipitation on the Geological Development of Badlands in Arid Regions. *Bull. Eng. Geol. Environ.* **2011**, *70*, 223–229. [CrossRef]

32. Paranthaman, R.; Azam, S. Effect of Composition on Engineering Behavior of Clay Tills. *Geosciences* **2021**, *11*, 427. [CrossRef]

33. Azam, S.; Khan, F. Geohydrological Properties of Selected Badland Sediments in Saskatchewan, Canada. *Bull. Eng. Geol. Environ.* **2014**, *73*, 389–399. [CrossRef]

34. Khan, F.S.; Azam, S. Determination of the Desiccation Behavior of Clay Slurries. *Int. J. Min. Sci. Technol.* **2017**, *27*, 981–988. [CrossRef]

35. Holtz, R.D.; Kovacs, W.D.; Sheahan, T.C. *An Introduction to Geotechnical Engineering*, 2nd ed.; Prentice-Hall: Englewood Cliffs, NJ, USA, 2011; Volume 733.

36. Moore, D.M.; Reynolds, R.C. *X-Ray Diffraction and the Identification and Analysis of Clay Minerals*; Oxford University Press (OUP): Oxford, UK, 1989.

37. Hendershot, W.H.; Lalande, H.; Duquette, M. Chapter 18. Ion Exchange and Exchangeable Cations. In *Soil Sampling and Methods of Analysis*; Canadian Society of Soil Science: Pinawa, MB, Canada; CRC Press: Boca Raton, FL, USA, 2008; pp. 173–178.

38. Khan, F.S.; Azam, S. Determination of Swelling Potential of a Fissured Expansive Clay in a Large Cell. In Proceedings of the 67th Canadian Geotechnical Conference, Regina, SK, Canada, 30 September 2014.

39. Gottardi, G. The Genesis of Zeolites. *Eur. J. Mineral.* **1989**, *1*, 479–488. [CrossRef]

40. Wilson, M.J.; Deer, W.A.; Howie, R.A.; Zussman, J. *Rock-Forming Minerals. 3C: Sheet Silicates. Clay Minerals*; Geological Soc.: London, UK, 2013.

41. Khan, F.M. Engineering Properties of Badlands in Semi-Arid Regions. Master's Thesis, The University of Regina (Canada), Regina, SK, Canada, 2012.

42. Azam, S. Solid-Liquid Separation of Laterite Slurries. Ph.D. Thesis, Faculty of Graduate Studies and Research, University of Alberta, Edmonton, AB, Canada, 2003.

43. Azam, S.; Abduljauwad, S.N.; Al-Shayea, N.A.; Al-Amoudi, O.B. Effects of Calcium Sulfate on Swelling Potential of an Expansive Clay. *Geotech. Test. J.* **2000**, *23*, 389–403.

44. Smykatz, K. *Differential Thermal Analysis. Application and Results in Mineralogy*; Springer: Berlin/Heidelberg, Germany, 1974.

45. Lehmann, P.; Merlin, O.; Gentine, P.; Or, D. Soil Texture Effects on Surface Resistance to Bare-Soil Evaporation. *Geophys. Res. Lett.* **2018**, *45*, 10–398. [CrossRef]

46. Bedient, P.B.; Huber, W.C.; Vieux, B.E. *Hydrology and Floodplain Analysis*, 5th ed.; Pearson Education Limited: Edinburgh, UK, 2013.

47. Yang, F.; Su, D.; Ma, Y.; Feng, C.; Yang, A.; Wang, M. Refraction Correction of Airborne LiDAR Bathymetry Based on Sea Surface Profile and Ray Tracing. *IEEE Trans. Geosci. Remote Sens.* **2017**, *55*, 6141–6149. [CrossRef]

48. Tommasi, P.; Boldini, D.; Caldarini, G.; Coli, N. Influence of Infiltration on the Periodic Re-Activation of Slow Movements in an Overconsolidated Clay Slope. *Can. Geotech. J.* **2013**, *50*, 54–67. [CrossRef]
49. Ting, L.; Chaosheng, T.; Dan, X.U.; Yunsheng, L.I.; Yan, Z.; Kan, W.; Bin, S.H.I. Advance on the engineering geological characteristics of expansive soil. *J. Eng. Geol.* **2018**, *26*, 112–128. [CrossRef]
50. Udukumburage, R.S.; Gallage, C.; Dawes, L. Oedometer Based Estimation of Vertical Shrinkage of Expansive Soil in a Large Instrumeted Soil Column. *Heliyon* **2019**, *5*, e02380. [CrossRef]
51. Umezaki, T.; Kawamura, T. Shrinkage and Desaturation Properties during Desiccation of Reconstituted Cohesive Soil. *Soils Found.* **2013**, *53*, 47–63. [CrossRef]